Stereodynamics of Adiabatic and Non-adiabatic Energy Transfer in a Molecule Surface Encounter

Yaolong Zhang[1‡], Connor L. Box[2‡], Tim Schäfer[3,4], Alexander Kandratsenka[3,4], Alec M. Wodtke[3,4], Reinhard J. Maurer[2*], and Bin Jiang[1*]

[1]*Department of Chemical Physics, School of Chemistry and Materials Science, Key Laboratory of Surface and Interface Chemistry and Energy Catalysis of Anhui Higher Education Institutes, University of Science and Technology of China, Hefei, Anhui 230026, China*

[2]*Department of Chemistry, University of Warwick, Gibbet Hill Road, Coventry, CV4 7AL, United Kingdom*

[3]*Institute for Physical Chemistry, Georg-August University of Göttingen, Göttingen, 37077, Germany*

[4]*Department of Dynamics at Surfaces, Max Planck Institute for Biophysical Chemistry, Göttingen, 37077, Germany*

‡: these authors contribute equally to the work.

*: corresponding authors: r.maurer@warwick.ac.uk; bjiangch@ustc.edu.cn

Abstract

Molecular energy transfer and reactions at solid surfaces depend on the molecular orientation relative to the surface. While such steric effects have been largely understood in electronically adiabatic processes, the orientation-dependent energy transfer in NO scattering from Au(111) was complicated by electron-mediated nonadiabatic effects, thus lacking a clear interpretation and posing a great challenge for theories. Herein, we investigate the stereodynamics of adiabatic and nonadiabatic energy transfer via molecular dynamics simulations of NO(v=3) scattering from Au(111) using realistic initial orientation distributions based on accurate neural network fitted adiabatic potential and electronic friction tensor. Our results reproduce the observed stronger vibrational relaxation for N-first orientation and enhanced rotational rainbow for O-first orientation, and demonstrate how adiabatic anisotropic interactions steer molecules into the more attractive N-first orientation to experience more significant energy transfer. Remaining disagreements with experiment suggest the direction for further developments of nonadiabatic theories for gas-surface scattering.

Keywords

Stereodynamics, Steering effect, Potential energy surface, Non-adiabatic energy transfer, Electronic friction

Introduction

Molecules colliding at solid surfaces can lead to energy flow among various molecular and surface degrees of freedom (DOFs), which is of fundamental importance to reactive dynamics at surfaces and energy transport across interfaces. The underlying dynamics of molecular energy conversion at gas-surface interfaces are dependent not only on the incidence energy (E_i) and the initial state of the molecule but also on the molecular orientation[11]. Quantum state-resolved experiments have revealed the orientation dependence of energy transfer and reactivity in various gas-surface systems[1-7], serving as a probe of the anisotropic molecule-surface interactions. Such steric effects have been mostly investigated in electronically adiabatic processes. For example, the alignment-dependent reactivity in activated dissociative adsorption observed experimentally[3-5] has been often interpreted by the molecular alignment with respect to the transition state on the adiabatic interaction potential[8-12]. Strong anisotropic interaction has also been found to control the unusual sticking and scattering of CO at Ru(0001)[13]. In comparison, the stereodynamics of non-adiabatic energy transfer at gas-surface interfaces involving electron-hole pair excitations is a much more subtle process that is less well understood.

Vibrationally inelastic scattering of NO from Au(111) represents a prototypical example of non-adiabatic energy transfer between a molecule and a metal surface[14-23] The observed multi-quantum vibrational relaxation and excitation of NO scattered from Au(111) can hardly be understood in an adiabatic picture and indicates remarkable nonadiabaticity in this system[14, 16]. More recent quantum state resolved measurements of NO scattering from Au(111) acquired for a wide range of initial conditions have provided a more complete picture of the energy transfer dynamics of this system[17-23]. In particular, oriented molecular beam experiments have shown that the vibrational relaxation of NO scattering from Au(111) can be strongly orientation-dependent[18, 21, 22, 24]. This system thus presents an excellent

benchmark for testing theoretical models of stereodynamics associated with non-adiabatic energy transfer.

Since a full-quantum dynamical simulation is infeasible in such a complex system, various approximate models have been developed differing in their treatments of the nonadiabatic effects[25-30], including an independent electron surface hopping (IESH) approach based on an effective Hamiltonian that describes molecule-metal hybridization and charge transfer in the presence of the metal electron continuum[26, 27] and an electronic friction (EF) method which convolutes the electronic response to the nuclear motion into a frictional force that acts on the nuclei[31]. The first reported comparison between the IESH and experimental results was quite encouraging[16, 28]. Nevertheless, it was later realized that the parametrized IESH Hamiltonian led to an unphysically attractive adiabatic potential energy surface (PES) and an exaggeration of the role of multi-bounce trajectories[19]. This inaccuracy in the adiabatic PES was argued to be responsible for the earlier fortuitous agreement with experiments at low E_i, but other disagreements with experimental observations were later discovered for different conditions[19, 20]. For example, although the IESH model qualitatively predicted that the vibrational relaxation preferentially occurs when the NO molecule hits the surface with the N atom facing down[28], the "overly attractive" adiabatic interaction eliminated any steric effects when simulating realistic molecular orientation distributions[32].

Recently, a more realistic neural network (NN) adiabatic PES of NO + Au(111) with a high barrier for NO dissociation has been developed based on thousands of density functional theory (DFT) data points[33]. Adiabatic Born Oppenheimer molecular dynamics (BOMD) simulations on this PES led to a large amount of vibrational energy of NO(v_i=15 or 16) transferring to other nuclear DOFs[33, 34], as the molecular vibration softens when

accessing the barrier by which its couplings with translation/rotation and surface phonons are greatly increased[32] . Further MD simulations with EF (MDEF) based on the NN representation of Kohn-Sham orbitals (hereafter referred as orbital-dependent friction, ODF) and fitted by NNs have correctly captured the nonadiabatic energy loss for low vibrational states of NO (v_i=2 or 3) in reproducing the single-quantum vibrational relaxation as a function of translational incidence energy[35]. These findings underscore the importance of accurately modelling both adiabatic and nonadiabatic energy transfer in this system[36]. These advanced methods now allow us to investigate the stereodynamics of realistically oriented NO(v_i=3) molecules scattering from Au(111) in the same manner.

Theoretical Methods

Molecular Dynamics Simulations with Electronic Friction

While the electron-nuclear nonadiabatic coupling is assumed to be weak[19], electronic degrees of freedom (DOFs) can be described via a frictional damping force representing the nonadiabatic linear response of electrons to the motion of adsorbate nuclei[31, 37]. This results in a generalized Langevin equation, which, within the Markov approximation and in the constant coupling limit, can be expressed as molecular dynamics (MD) with electronic friction (MDEF)[31],

$$m_i \frac{\partial^2 r_i}{\partial t^2} = -\frac{\partial V(\mathbf{r})}{\partial r_i} - \sum_j \Lambda_{ij} \frac{\partial r_j}{\partial t} + \mathbf{R}_i(t)\,. \qquad (1.)$$

In Eq (1), m is the nuclear mass, r (=x or y or z) is the nuclear DOF, $V(\mathbf{r})$ is the adiabatic ground state potential energy surface (PES) as a function of all nuclear positions, $\mathbf{\Lambda}$ is the electronic friction tensor (EFT) couples different nuclear DOFs, $\mathbf{R}$ is a Gaussian random force, subscripts i and j run over these atoms in the adsorbate. In practice, the EFT can be calculated from Kohn-Sham density functional theory (DFT) orbitals via time-dependent

perturbation theory.[38] This full-rank EFT is referred as orbital-dependent friction (ODF). The MDEF approach offers an effective framework for describing both adiabatic and nonadiabatic energy transfer between molecules and metal surfaces.[39-42] A widely-used local density friction approximation was not employed here[43, 44], because its effect was found to be negligible in NO+Au(111) system[33]. While the electronic friction is neglected, the MDEF simulation is reduced to the Born-Oppenheimer MD (BOMD) case within the adiabatic approximation. By comparing MDEF and BOMD results, we are able to estimate the relative importance of the nonadiabatic effects.

Potential Energy Surface and Electronic Friction Tensor Representations

The adiabatic PES and the tensorial ODF representation for the NO + Au(111) system have been published elsewhere[35], based on the scalar[45, 46] and tensorial[47] versions of embedded atom neural network (EANN) approach, respectively. Briefly, in the EANN framework, the total energy is decomposed into the summation of atomic energies, *i.e.*, $E = \sum_{i=1}^{N} E_i$, each of which is given by a function of the embedded atom density (EAD) feature vector ($\boldsymbol{\rho}^i$) of the corresponding center atom. An atomic neural network serves as the mapping function from an EAD vector to an atomic energy. For simplicity, $\boldsymbol{\rho}^i$ can be evaluated by the square of the linear combination of a series of Gaussian-type orbitals (GTOs) at all neighbor atoms,

$$\rho^i = \sum_{l_x,l_y,l_z}^{l_x+l_y+l_z=L} \frac{L!}{l_x!l_y!l_z!}\left(\sum_{j\neq i}^{N_c} c_j \varphi(\hat{\mathbf{r}}_{ij})\, f_c(r_{ij})\right), \tag{2.}$$

where $\varphi(\hat{\mathbf{r}}_{ij})$ is a GTO in the Cartesian coordinate frame, c_j is the orbital coefficient, and $f_c(r_{ij})$ is a cutoff function to decay the local interaction to zero at r_c. Specifically,

$$\varphi(\hat{\mathbf{r}}_{ij}) = x_{ij}^{\,l_x} y_{ij}^{\,l_y} z_{ij}^{\,l_z} \exp\left(-\alpha(r_{ij} - r_s)^2\right), \tag{3.}$$

where $\hat{\mathbf{r}}_{ij} = \hat{\mathbf{r}}_j - \hat{\mathbf{r}}_i$, $x_{ij} = x_j - x_i$, $y_{ij} = y_j - y_i$, and $z_{ij} = z_j - z_i$ are the position vector and its three components of a neighbor atom *j* relative to the central atom *i*, with r_{ij} being the interatomic distance, α and r_s are parameters that control the radial distribution of the GTO, $l_x+l_y+l_z=L$ specifies the orbital angular momentum (L). The PES is obtained by optimizing network parameters to minimize the deviations between the sum of atomic NNs (and its derivatives with respect to atomic coordinates) and the DFT energy (and atomic forces).

Differing from the scalar energy, EFT is a 2-order rank tensor that is covariant with respect to rotation and permutation of atoms in the adsorbate, which has to be adapted in the EANN representation[47]. To this end, two matrices are introduced to mimic the EFT formulation. Considering an adsorbate with N atoms, a $3N \times M$ matrix ($\mathbf{D}^{\mathrm{NN}_1}$) is constructed as the first-order derivatives of an EANN output vector (**H)** with respect to atomic Cartesian coordinates of the adsorbate (**r)**,

$$\mathbf{D}^{\mathrm{NN}_1} = \sum_{i=1}^{N} \frac{\partial \mathbf{H}}{\partial \boldsymbol{\rho}_i} \frac{\partial \boldsymbol{\rho}_i}{\partial \mathbf{r}}. \tag{4.}$$

where **H** contains M components (M should be no less than $3N$). The other $3N \times 3N$ second-order derivative matrix ($\mathbf{D}^{\mathrm{NN}_2}$) is expressed as,

$$\mathbf{D}^{\mathrm{NN}_2} = \sum_{i=1}^{N} \sum_{l=1}^{n_{orb}} \mathbf{S}^{il} F^{il}, \tag{5.}$$

where $\mathbf{S}^{il}$ is the second-order derivative matrix of $\boldsymbol{\rho}^{il}$ (the *l*th elements in EAD of the *i*th atom) with respect to **r** and F^{il} is first-order derivative of an EANN scalar output with

respect to $\boldsymbol{\rho}^{il}$. Multiplying $\mathbf{D}^{\mathrm{NN}_1}$ and $\mathbf{D}^{\mathrm{NN}_2}$ with their own transpose matrix results in two $3N \times 3N$ matrices that naturally guarantee the rotational covariance and positive semidefiniteness of the EFT,

$$\boldsymbol{\Lambda}^{\mathrm{NN}} = \mathbf{D}^{\mathrm{NN}_1}(\mathbf{D}^{\mathrm{NN}_1})^{\mathrm{T}} + \mathbf{D}^{\mathrm{NN}_2}(\mathbf{D}^{\mathrm{NN}_2})^{\mathrm{T}} \tag{6.}$$

In practice, $\mathbf{D}^{\mathrm{NN}_1}$ and $\mathbf{D}^{\mathrm{NN}_2}$ rely on two different EANNs and the resultant $\boldsymbol{\Lambda}^{\mathrm{NN}}$ is used in the loss function to optimize all parameters simultaneously.

DFT calculations

Periodic DFT calculations were performed to generate the training data of energies, forces, and ODF tensors ($\boldsymbol{\Lambda}$), respectively. We have performed spin-polarized DFT calculations for the NO + Au(111) system using VASP[48, 49] with the PW91 functional[50]. The Au(111) surface was represented by a four-layer slab model in a 3×3 unit cell with the top two layers movable. The Brillouin zone was sampled by a 4×4×1 Gamma-centered ***k***-point grid. A total of 2722 points with both energies and forces were collected mainly from direct dynamics trajectories to represent the adiabatic PES. The 6×6 ODF EFT was computed using our implementation within the all-electron numerical atomic orbital code FHI-Aims[38, 51]. With the same slab model as the PES, a finite difference approach (a Cartesian displacement of 0.0025 Å was used) was employed to evaluate the first order response of Hamiltonian and overlap matrices. At each displacement, a self-consistent DFT calculation was carried out using the PBE functional[52]. A standard 'tight' numerical basis set was employed with a 9×9×1 k-point mesh. The EFT was evaluated using a Gaussian smearing function of width 0.6 eV and a Fermi factor corresponding to an electronic temperature of 300 K. The use of a broadening width of 0.6 eV is partially justified by roughly converging

the magnitude of friction coefficients within ±10%.[35] More details can be found in Refs. [33] and [35].

Initial Conditions

In this work, BOMD and MDEF simulations were performed with a well-defined initial orientation of the NO molecule, in addition to the conventional quasi-classical initial conditions[53]. The NO molecules were initialized from 6.0 Å above the surface with the molecular center of mass in the 3×3 unit cell. The initial vibrational momentum of the NO molecule was selected using the standard Monte-Carlo sampling for a given vibrational action number (v_i). For isotropic calculations, the NO molecule was considered as a rigid rotor and its rotational angular momentum, $\vec{\boldsymbol{J}} = \sqrt{J_i(J_i+1)}\hbar$ associated with the rotational quantum number J_i was perpendicular to the molecule, followed by a random orientation of NO before impinging to the surface along the surface normal at a given incidence energy. For N-first and O-first orientations, both quantum and classical angular distributions have been sampled. Quantum mechanical angular distributions were sampled by a rejection sampling method. Classically, the molecule is approximated as a symmetric top whose rotational angular momentum vector (equivalently $\vec{\boldsymbol{J}}$ in Fig. 1a, as the electronic angular momenta are neglected) is no longer perpendicular to the molecule having its projections on the space-fixed *Z* axis and the molecular *z* axis. Accordingly, the $\vec{\boldsymbol{J}}$ vector of the NO molecule was oriented so that its angle about the *Z* axis is given by $\cos\alpha = \sqrt{3}/3$ and about the molecular axis by $\cos\beta = \sqrt{3}/3$.[38] On the other hand, the Au(111) surface was first equilibrated to 300 K for 5 ps by the Andersen thermostat[54], after which the snapshots were randomly selected as initial configurations associated with their velocities in subsequent molecular scattering calculations. The final vibrational action numbers v_f was determined by the Einstein-Brillouin-Keller (EBK) semi-classical

quantization. The final rotational quantum number j_f was derived from the rotational angular momentum using the relationship above. These quantum numbers are finally rounded into their closest integers via the standard histogram binning procedure.

Results and Discussion

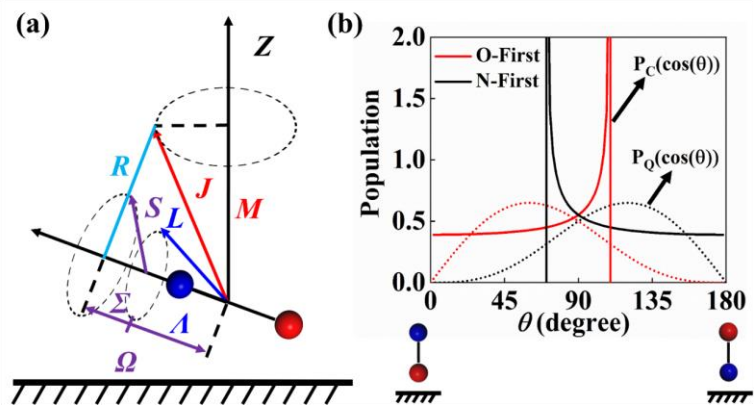

Fig. 1. (a) Vectorial relationship of the electronic ($\vec{\boldsymbol{L}}$), spin ($\vec{\boldsymbol{S}}$), and total ($\vec{\boldsymbol{J}}$) angular momenta, and their projections on the molecular axis and space-fixed *Z* axis. (b) Classical (P_C) and quantum (P_Q) angular distributions for N-first and O-first orientations of NO.

A meaningful comparison between MD and experimental data of oriented molecules requires proper sampling of the initial orientation distribution. In experiments, the $X^2\Pi_{1/2}$(v_i=3, J=Ω=0.5) state of the polar NO molecule was optically selected and oriented via the Stark effect in an electric field[55], for which the molecular orientation is quantified by the angle (θ) between the electric field acting along the space-fixed *Z* axis and dipole moment lying along the molecule-fixed (internuclear) *z* axis. This open shell molecule obeys Hund's case (*a*)[56], whose angular momenta are illustrated in Fig. 1a. Here, $\vec{\boldsymbol{L}}$ and $\vec{\boldsymbol{S}}$ are the electronic and spin angular momenta with their projections on the *z* axis $\vec{\boldsymbol{\Lambda}}$ and $\vec{\boldsymbol{\Sigma}}$, the nuclear rotation angular momentum $\vec{\boldsymbol{R}}$ is directed perpendicular to the *z* axis, and

$\vec{J}$ is the total angular momentum which makes its projection $\vec{M}$ on the space-fixed *Z* axis and $\vec{\Omega} = \vec{\Lambda} + \vec{\Sigma}$ on the molecule-fixed *z* axis.

Quantum mechanically, the so-called N-first and O-first orientations in experiments[21, 24] correspond to angular distributions of rotational wave functions with $J=\Omega=|M|=0.5$, or explicitly expressed as $P_+(\cos\theta) = (1+\cos\theta)/2$ and $P_-(\cos\theta) = (1-\cos\theta)/2$, respectively,[32] as shown in Fig. 1b. Classically, since electronic DOFs are neglected in our model, the molecule is approximated by a symmetric top, for which the $\vec{J}$ vector is oriented to have projections on both the space- and molecule-fixed axes with its angle about the *Z* axis being $\cos\alpha = M/\sqrt{J(J+1)}$ and about the *z* axis being $\cos\beta = \Omega/\sqrt{J(J+1)}$.[57] The resultant quantum and classical distributions for N-first and O-first orientations are shown in Fig. 1b. Although the quantum and classical angular distributions look quite different, their averages (or expectation values), *i.e.*, $\langle\cos\theta\rangle = M\Omega/J(J+1)$, are identical[57]. In practical MD calculations, classical sampling of rotational angular momenta has been more frequently applied, which, for example, has led to good agreement with quantum and/or experimental results on steric effects of molecular dissociation on metal surfaces[9, 10, 12, 58, 59]. Here we sample both quantum and classical angular distributions and the respective simulation results are quite similar.

We first compare the calculated and measured final state distributions for the scattering of oriented NO(v_i=3) from Au(111) at surface temperature T_s=300 K, and high incidence energy (E_i≈0.96 eV) in Fig. 2, where both experimental and IESH results are available. Note that although theories predict minor populations for v_f=0 or v_f>v_i, they have not been measured due to experimental limitations or scope, which will thus not be discussed here. The experimental data[32] (Fig. 2a and Fig. 2e) clearly show that N-first orientation leads to more inelastic scattering, and a rotationally cold distribution. On the other hand, initial O-

first orientation leads to less vibrational inelasticity, but a much hotter rotational distribution with a remarkable rotational rainbow peak around $J_f \approx 40$ in the vibrationally elastic scattering channel (v_i=3→v_f=3). Early analysis of IESH trajectories suggested that multi-quantum vibrational energy loss primarily takes place while the NO molecule orients its N-end towards the surface[28]. However, IESH results considering the experimental-like (quantum) angular distributions extracted from Ref. 32 (referred to as IESH) not only fail to predict any steric dependence but underestimate the vibrational inelasticity and give too broad final rotational state (J_f) distributions with no bimodal structure (Fig. 2b and Fig. 2f). This failure is at least partially due to the "too attractive" adiabatic PES used in the IESH model, which results in too much multi-bounce with the surface and therefore too facile reorientation of the molecule[32].

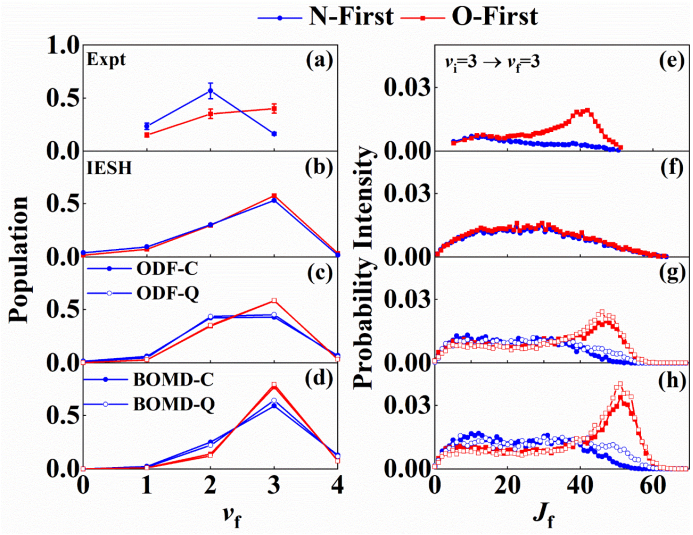

Fig. 2 Comparison of final vibrational (a-d) and rotational (e-h, v_i=3 → v_f=3) state distributions of NO(v_i=3) scattering from Au(111) at T_s=300 K with translational incidence energies, E_i = 0.96 eV for N-First (circles) and O-First (squares) orientations, including experimental (a and e)[32], IESH[32] (b, f), ODF (c, g), BOMD (d, h) results. Filled (open) symbols correspond to results based on classical (quantum) rotational initial state distributions.

The NN-PES used in this work largely removes the artefacts observed in the IESH simulations. Whereas BOMD results yield a vibrational final state distribution for O-first and N-first that is largely similar to that of IESH (Fig. 2d), significantly underestimating vibrationally inelastic events, MDEF results reported in Fig. 2c show significantly higher probability for (v_i=3 → v_f=2) scattering in both N-first and O-first orientations. In the case of N-first, this yields more scattering events with (v_i=3 → v_f=2) than (v_i=3 → v_f=3), which is qualitatively in line with experiment. Therefore, MDEF correctly predicts more nonadiabatic vibrational energy loss in the N-first orientation than in the O-first orientation. This behavior is observed when sampling from quantum (ODF-Q) or classical (ODF-C) angular distributions. As already previously reported,[35] MDEF predicts too little multi-quantum vibrational energy loss (v_i=3 → v_f=1), which is likely due to an underestimation of nonadiabatic effects when scattering events occur close to the surface. We will discuss in more detail below.

When considering rotational final state distributions shown in Fig 2 on the right, both the adiabatic BOMD results shown in Fig. 2h and the MDEF results shown in Fig. 2g feature a rotational rainbow effect for O-first scattering events, which was not captured in the IESH results. Again, this is largely independent of the type of angular distribution from which trajectories are sampled. The BOMD results on the new NN-PES capture the steric effects (Fig. 2d and Fig. 2h), although the degree of vibrational relaxation is apparently underestimated and the rotational rainbow is shifted to higher J_f values, due to the neglect of nonadiabatic vibrational energy transfer. The weak nonadiabatic effects captured with the MDEF simulations lead to a shift of the rotational final state distribution to lower J_f values. While this brings the results closer to experiment, final rotational states remain too high. The overestimation of the final rotational states could potentially be a consequence of the overestimation of trapping on the current NN-PES[35], but the rotational state

distributions are barely changed when only accounting for single bounce effects. (See Fig. S1 in the Electronic Supporting Information (ESI†)). Overall, the new MDEF results provide a significant improvement in the description of both the vibrational and rotational final state distributions, yet the strong orientational dependence of the vibrational relaxation, *i.e.* the difference in vibrationally elastic and inelastic scattering for O-first and N-first events, remains underestimated when compared to experiment. This deficiency will be discussed below.

Fig. 3 presents a more comprehensive comparison between experiment[21, 32] and ODF-C results for NO(v_i=3→v_f=2 and 3) scattering from Au(111) varying the incidence energy from E_i=0.27 to 0.89 eV. ODF-Q results are again rather similar and shown in the ESI† along with BOMD ones (See Figs. S2-S3 in the ESI†). We first note that the vibrational populations shown in the insets are in good agreement with experiment for the O-first orientation in the adiabatic (left) and nonadiabatic channel (right) across all translational incidence energies (increasing from bottom to top). Vibrational populations as predicted by MDEF for the N-first orientation are overestimated in the elastic channel and underestimated in the inelastic channel. Breaking the vibrational final state populations further down into rotational final states shows clear steric- and incidence-energy-dependence of rotational final distributions. In the vibrationally elastic channel, the rotational rainbow in the O-first orientation in experiment is well captured by MDEF. It shifts towards lower J_f and gradually disappears as E_i decreases (from top to bottom); this is accompanied by a weakening of the dependence of rotational state distributions on initial orientation, *i.e.* the difference between N-first and O-first disappears. The rotational state distribution in the elastic N-first channel is not so well represented compared to experiment. In the vibrationally inelastic channel (right column of Fig. 3), the experiment shows a smaller difference between N-first and O-first rotational final states and no rotational

rainbow appears for O-first. Here, MDEF incorrectly predicts a broad vibrational rainbow for O-first at high incidence energies. On the other hand, MDEF is in better agreement with experiment for the N-first channel. While BOMD (see Fig. S3 in the ESI†) heavily underestimates the inelastic channel with no rotational rainbows present, MDEF overestimates the rotational rainbow structures at high E_i. The origin of this effect will be discussed next.

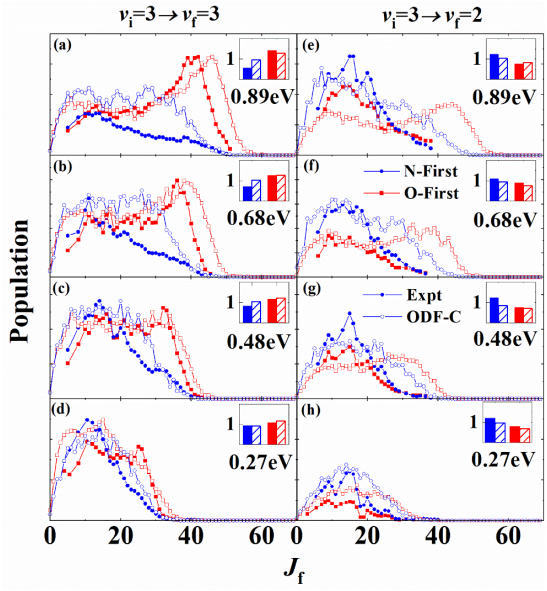

Fig. 3 Comparison of experimental (filled) and theoretical (the ODF-C model, open) final rotational state distributions of vibrationally elastic (v_f=3) and inelastic (v_f=2) scattering of NO(v_i=3) from Au(111) with translational incidence energies, E_i ranging from 0.27 to 0.89 eV for N-first (blue) and O-first (red) orientations. At each E_i, calculated rotational state distributions in both channels are multiplied by the same factor so that the highest theoretical peak matches the highest experimental one. The inset in each panel shows the experimental (filled) and theoretical (slashed) ratios of the final vibrational state population with N-first (blue) and O-first (red) orientations relative to that with the isotropic orientation.

To better understand the correlation between the observed steric effects and the molecule-surface interactions, we analyse the trajectories with different initial orientations on the adiabatic PES and present results in Fig. 4. Specifically, the adiabatic PES is more attractive when the N atom (rather than the O atom) is oriented towards the surface and features an adsorption well with a tilted N-first geometry at $\theta \approx 125^{\circ}$ (Fig. 4a). This anisotropic interaction will induce a strong torque when the NO molecule impacts at the surface with its O-end. This leads to high rotational excitation upon scattering (*e.g.* $J_f > 35$ See Fig. S4 in the ESI†). This is the fundamental cause of the rotational rainbow appearing for the O-first orientation, similar to prior reports of rotational rainbows[2, 60, 61]. By contrast, the molecule striking at the surface with its N-end would feel a more attractive force hindering its rotational motion, thus favoring lower rotational excitation. Interestingly, we find that a fraction of trajectories with the initial O-first orientation reorient the N-end down to the surface when collision occurs, manifesting some dynamical steering even at this high E_i. These reoriented trajectories coincide with those initiated with the N-first orientation in terms of their turning points in the configuration space, as shown in Fig. 4a. This explains the similar low-J_f distributions for both O-first and N-first orientations. Apparently, the previous IESH model based on an inferior adiabatic PES[33] substantially overestimates this reorientation effect, thus eliminating any steric dependence even at a high incidence energy. Note that the inaccuracy of the previous PES was mainly due to the fact that the empirical functions used to fit the PES were not sufficiently flexible to globally describe the NO+Au(111) system, especially the couplings between molecular vibrations and surface phonons when the molecular bond is stretched[33]. The DFT calculations to generate both PESs are actually at the generalized gradient approximation (GGA) level.

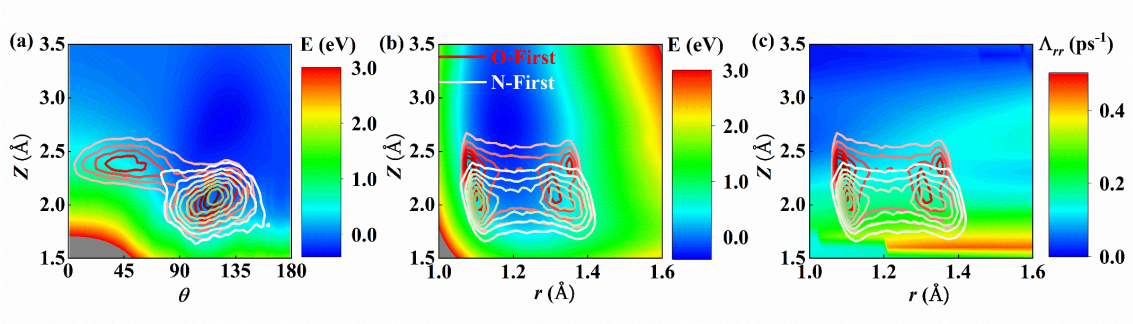

Fig. 4 Contour plots of the NO geometries of closest approach to the surface for ODF-C trajectories with two initial orientations: N-first (white) and O-first (red) with E_i =0.89 eV. (a) values of the NO centre-of-mass altitude above surface (Z) and the orientational angle (θ) are shown superimposed on a 2D cut of the NN-PES (colors). (b) values of Z and NO bond length (r) are shown superimposed on a 2D cut of the NN-PES (colors). (c) the trajectory inner turning points are shown superimposed on the NN-ODF diagonal element (Λ_{rr}) as a function of Z and r (colors) (panel c). Note that the 2D cut of the NN-PES is obtained with all other molecular coordinates optimized on the PES and the surface configuration fixed at the adsorption state. These contours are the kernel density maps of the impact points of corresponding trajectories indicating the spatial and population distributions of the impact points. The white and red colors are associated with the initial orientations of N-first and O-first, respectively. For each initial orientation, a darker color associates with a higher population at the corresponding location. Similar kernel density maps are shown in Figs. S4-S6 in the ESI†.

More importantly, these trajectories for the N-first orientation (including the ones reoriented to the N-first orientation from an initial O-first orientation) could approach the surface much closer, which at the same time leads to a significantly elongated NO distance compared to molecules with an O-first orientation (Fig. 4b). In such cases, more significant vibrational softening occurs and vibrational energy can be transferred to surface phonons,

as discussed in our previous work[33, 34]. Likewise, such trajectories are subject to stronger EF forces due to larger nonadiabatic couplings associated with the NO bond stretching at higher metal electron densities closer to the surface (see, for example, the ODF element along the molecular vibration (Λ_{rr}) in Fig. 4c), giving rise to more nonadiabatic vibrational energy transfer to electron-hole pairs[35, 40, 41]. Both effects contribute to the higher vibrational relaxation probability for N-first orientation than for O-first orientation. These results together confirm the presence of an angular filtering effect of rotational cooling via vibrational relaxation when the molecule impacts the surface with its N-end, as proposed in the experimental work[21]. Interestingly, we find that as E_i decreases, all molecules are less likely to approach the surface sufficiently close to experience the anisotropic interaction and the barrier[33], so that they tend to scatter in a rotationally cool end state having overall experienced less vibrational energy loss. As a result, the steric effect is weaker for low E_i. The weaker vibrational inelasticity and rotational excitation at lower E_i were observed in experiments[19] and are well reproduced by the current theory.

More explicit correlations between the initial orientation and final states can be seen in (See Figs. S5-S6 in the ESI†), where trajectories corresponding to different final vibrational states are separately shown for both BOMD and MDEF simulations. Specifically, adiabatic BOMD trajectories indicate a pure angular filter for vibrational relaxation (See Fig. S5 in the ESI†). This means that a molecule with an initial O-first orientation must reorient to an N-first orientation to trigger vibrational relaxation. Such inelastic O-first trajectories are more likely to rearrange and to come closer to the channel, following more closely the behaviour of the N-first trajectories. In comparison, vibrational relaxation can occur at high E_i even for molecules remaining in the unfavorable O-first orientation in MDEF simulations because of the additional nonadiabatic energy loss (See Fig. S6 in the ESI†). Molecules relaxed to (v_f = 2) in this scenario experience more or less the same paths as

their elastically scattered counterparts, which leads unexpectedly to a rotational rainbow feature in the vibrationally inelastic channel of the corresponding ODF results (See Fig. 3 and Fig. S2 in the ESI†).

In light of the above analysis, we argue that the new NN PES properly describes the adiabatic anisotropic interaction between NO and the Au(111) surface, which is neither too strong to retain the initial molecular orientation, as in the previous PES used in the IESH model, nor too weak to differentiate two opposite orientations. The steric effect is driven by this adiabatic anisotropic interaction, which can guide some N-first trajectories to get closer to the surface and become more influenced by the non-adiabatic effects than the O-first ones. Quantitatively, however, the current ODF model seems to overestimate (underestimate) the nonadiabatic couplings of the O-first (N-first) oriented configurations (Note that our MDEF-ODF calculations did reproduce well the scattering probabilities of NO(v_i=3→v_f=2 and 3) for an isotropic orientation as a function of E_i[35]). It is at least partially evidenced, where Λ_{rr} is approximately symmetric with respect to the orientational angle (See Fig. S7 in the ESI†**)** so that the difference between the non-adiabatic energy losses for the two orientations is not as large as expected. This results in a weaker steric effect than that observed in experiment and the artificial rotational rainbow structures in the v_f=3 channel in the ODF model. The agreement with experiment may be improved by implementing strongly-coupled nonadiabatic dynamical theories such as IESH, yet necessarily combined with accurate first-principles adiabatic (and diabatic) PESs. Previous empirical one-dimensional potentials for the neutral and anionic NO perpendicular to Au(111) already showed that the energy required for charge transfer is lower when the N-atom points to the surface, implying a steric dependence of nonadiabatic energy transfer[18].

Conclusion

To summarize, we present here extensive MDEF simulations based on first-principles-determined potential energy and electronic friction tensor landscapes, which provide a clear picture for understanding the experimentally observed steric effect in NO(v_i=3) scattering from Au(111). Our simulations confirm what was previously postulated by the experiment, namely that NO molecules are preferentially steered to an N-first orientation because of the anisotropic interaction, from which they are less likely to scatter with high rotational energy. In contrast, O-first scattering events lead to strong rotational excitation along with rotational rainbow characteristics. Remarkably, what we additionally reveal is that this strong stereodynamical steering effect is also coupled to nonadiabatic vibrational inelasticity as N-first molecules reach distances closer to the surface than O-first molecules where they exhibit nonadiabatic vibrational energy loss and are more likely to lose one or more vibrational quanta. Although our electronic friction based model still quantitatively underestimates the steric difference with regard to the nonadiabatic vibrational energy loss, it represents a big step towards a complete understanding to this problem as the steric effect was totally absent in simulations by a more advanced nonadiabatic theory based on an inferior PES. We conclude that only with the most accurate possible adiabatic PES can one accurately account for electronically nonadiabatic interactions in this important benchmark system and only once this is established can further improvements in nonadiabatic dynamics methods be targeted. A more advanced quantum treatment of the initial state and the state-to-state transitions could also improve the results and deserves further investigation.

Data availability

Additional results for analyzing the energy transfer mechanism are provided in the Electronic Supporting Information (ESI)†. The data that support the findings of this study are available from the corresponding author (B. J.) upon request.

Conflict of Interest

There is no conflicts to declare.

Funding Information

B.J. thanks the support from National Natural Science Foundation of China (22073089 and 22033007), Anhui Initiative in Quantum Information Technologies (AHY090200), CAS Project for Young Scientists in Basic Research (YSBR-005), the Fundamental Research Funds for the Central Universities (WK2060000017). C.L.B. is supported with an EPSRC-funded Ph.D. studentship. R.J.M. acknowledges funding from the UKRI Future Leaders Fellowship program (MR/S016023/1). Calculations have been done on the Supercomputing Center of USTC and Hefei Advanced Computing Center.

References

1. E. W. Kuipers, M. G. Tenner, A. W. Kleyn and S. Stolte, *Phys. Rev. Lett.*, 1989, **62**, 2152-2155.
2. E. W. Kuipers, M. G. Tenner, A. W. Kleyn and S. Stolte, *Nature*, 1988, **334**, 420-422.
3. H. Hou, S. J. Gulding, C. T. Rettner, A. M. Wodtke and D. J. Auerbach, *Science*, 1997, **277**, 80-82.
4. B. L. Yoder, R. Bisson and R. D. Beck, *Science*, 2010, **329**, 553-556.
5. M. Kurahashi and Y. Yamauchi, *Phys. Rev. Lett.*, 2013, **110**, 246102.
6. O. Godsi, G. Corem, Y. Alkoby, J. T. Cantin, R. V. Krems, M. F. Somers, J. Meyer, G.-J. Kroes, T. Maniv and G. Alexandrowicz, *Nat. Commun.*, 2017, **8**, 15357.
7. Y. Alkoby, H. Chadwick, O. Godsi, H. Labiad, M. Bergin, J. T. Cantin, I. Litvin, T. Maniv and G. Alexandrowicz, *Nat. Commun.*, 2020, **11**, 3110.
8. M.-N. Carre and B. Jackson, *J. Chem. Phys.*, 1998, **108**, 3722-3730.
9. F. Nattino, C. Díaz, B. Jackson and G.-J. Kroes, *Phys. Rev. Lett.*, 2012, **108**, 236104.
10. B. Jiang and H. Guo, *J. Phys. Chem. C*, 2016, **120**, 8220–8226.
11. B. Jiang, *Chem. Sci.*, 2017, **8**, 6662-6669.
12. R. Yin, Y. Zhang, F. Libisch, E. A. Carter, H. Guo and B. Jiang, *J. Phys. Chem. Lett.*, 2018, **9**, 3271-3277.
13. I. Lončarić, G. Füchsel, J. I. Juaristi and P. Saalfrank, *Phys. Rev. Lett.*, 2017, **119**, 146101.
14. Y. Huang, C. T. Rettner, D. J. Auerbach and A. M. Wodtke, *Science*, 2000, **290**, 111-114.
15. Y. Huang, A. M. Wodtke, H. Hou, C. T. Rettner and D. J. Auerbach, *Phys. Rev. Lett.*, 2000, **84**, 2985.
16. R. Cooper, C. Bartels, A. Kandratsenka, I. Rahinov, N. Shenvi, K. Golibrzuch, Z. Li, D. J. Auerbach, J. C. Tully and A. M. Wodtke, *Angew. Chem. Int. Ed.*, 2012, **51**, 4954-4958.
17. K. Golibrzuch, P. R. Shirhatti, J. Altschaffel, I. Rahinov, D. J. Auerbach, A. M. Wodtke and C. Bartels, *J. Phys. Chem. A*, 2013, **117**, 8750-8760.
18. N. Bartels, B. C. Kruger, D. J. Auerbach, A. M. Wodtke and T. Schafer, *Angew. Chem. Int. Ed.*, 2014, **53**, 13690-13694.
19. K. Golibrzuch, P. R. Shirhatti, I. Rahinov, A. Kandratsenka, D. J. Auerbach, A. M. Wodtke and C. Bartels, *J. Chem. Phys.*, 2014, **140**, 044701.
20. B. C. Kruger, N. Bartels, C. Bartels, A. Kandratsenka, J. C. Tully, A. M. Wodtke and T. Schafer, *J. Phys. Chem. C*, 2015, **119**, 3268-3272.
21. N. Bartels, K. Golibrzuch, C. Bartels, L. Chen, D. J. Auerbach, A. M. Wodtke and T. Schafer, *J. Chem. Phys.*, 2014, **140**, 054710.
22. B. C. Krüger, N. Bartels, A. M. Wodtke and T. Schäfer, *Phys. Chem. Chem. Phys.*, 2016, **18**, 14976-14979.
23. K. Golibrzuch, N. Bartels, D. J. Auerbach and A. M. Wodtke, *Annu. Rev. Phys. Chem.*, 2015, **66**, 399-425.
24. N. Bartels, K. Golibrzuch, C. Bartels, L. Chen, D. J. Auerbach, A. M. Wodtke and T. Schafer, *Proc. Natl. Acad. Sci. U.S.A.*, 2013, **110**, 17738-17743.
25. S. Li and H. Guo, *J. Chem. Phys.*, 2002, **117**, 4499.
26. S. Roy, N. A. Shenvi and J. C. Tully, *J. Chem. Phys.*, 2009, **130**, 174716.
27. N. Shenvi, S. Roy and J. C. Tully, *J. Chem. Phys.*, 2009, **130**, 174107.
28. N. Shenvi, S. Roy and J. C. Tully, *Science*, 2009, **326**, 829-832.
29. S. Monturet and P. Saalfrank, *Phys. Rev. B*, 2010, **82**, 075404.
30. T. Serwatka, G. Füchsel and J. C. Tremblay, *Phys. Chem. Chem. Phys.*, 2020, **22**, 6584-6594.
31. M. Head-Gordon and J. C. Tully, *J. Chem. Phys.*, 1995, **103**, 10137-10145.
32. N. Bartels, PhD PhD Thesis, University of Göttingen, 2015.
33. R. Yin, Y. Zhang and B. Jiang, *J. Phys. Chem. Lett.*, 2019, **10**, 5969-5974.
34. R. Yin and B. Jiang, *Phys. Rev. Lett.*, 2021, **126**, 156101.
35. C. L. Box, Y. Zhang, R. Yin, B. Jiang and R. J. Maurer, *JACS Au*, 2021, **1**, 164-173.

36. X. Zhou, G. Meng, H. Guo and B. Jiang, *J. Phys. Chem. Lett.*, 2022, **13**, 3450-3461.
37. B. Hellsing and M. Persson, *Phys. Scr.*, 1984, **29**, 360-371.
38. R. J. Maurer, M. Askerka, V. S. Batista and J. C. Tully, *Phys. Rev. B*, 2016, **94**, 115432.
39. R. J. Maurer, B. Jiang, H. Guo and J. C. Tully, *Phys. Rev. Lett.*, 2017, **118**, 256001.
40. P. Spiering and J. Meyer, *J. Phys. Chem. Lett.*, 2018, **9**, 1803-1808.
41. Y. Zhang, R. J. Maurer, H. Guo and B. Jiang, *Chem. Sci.*, 2019, **10**, 1089-1097.
42. P. Spiering, K. Shakouri, J. Behler, G.-J. Kroes and J. Meyer, *J. Phys. Chem. Lett.*, 2019, **10**, 2957-2962.
43. J. I. Juaristi, M. Alducin, R. Díez Muiño, H. F. Busnengo and A. Salin, *Phys. Rev. Lett.*, 2008, **100**, 116102.
44. M. Alducin, R. Díez Muiño and J. I. Juaristi, *Prog. Surf. Sci.*, 2017, **92**, 317-340.
45. Y. Zhang, C. Hu and B. Jiang, *J. Phys. Chem. Lett.*, 2019, **10**, 4962-4967.
46. Y. Zhang, J. Xia and B. Jiang, *J. Chem. Phys.*, 2022, **156**, 114801.
47. Y. Zhang, R. J. Maurer and B. Jiang, *J. Phys. Chem. C*, 2020, **124**, 186-195.
48. G. Kresse and J. Furthmuller, *Phys. Rev. B*, 1996, **54**, 11169-11186.
49. G. Kresse and J. Furthmuller, *Comp. Mater. Sci.*, 1996, **6**, 15-50.
50. J. P. Perdew, J. A. Chevary, S. H. Vosko, K. A. Jackson, M. R. Pederson, D. J. Singh and C. Fiolhais, *Phys. Rev. B*, 1992, **46**, 6671-6687.
51. V. Blum, R. Gehrke, F. Hanke, P. Havu, V. Havu, X. Ren, K. Reuter and M. Scheffler, *Comput. Phys. Comm.*, 2009, **180**, 2175-2196.
52. J. P. Perdew, K. Burke and M. Ernzerhof, *Phys. Rev. Lett.*, 1996, **77**, 3865-3868.
53. G. H. Peslherbe, H. Wang and W. L. Hase, *Adv. Chem. Phys.*, 1999, **105**, 171-201.
54. H. C. Andersen, *J. Chem. Phys.*, 1980, **72**, 2384-2393.
55. T. Schafer, N. Bartels, N. Hocke, X. M. Yang and A. M. Wodtke, *Chemical Physics Letters*, 2012, **535**, 1-11.
56. I. N. Levine, *Molecular Spectroscopy*, Wiley, New York, 1975.
57. S. E. Choi and R. B. Bernstein, *J. Chem. Phys.*, 1986, **85**, 150-161.
58. M. Kay, G. R. Darling and S. Holloway, *J. Chem. Phys.*, 1998, **108**, 4614-4627.
59. D. A. McCormack and G.-J. Kroes, *Phys. Chem. Chem. Phys.*, 1999, **1**, 1359-1374.
60. F. H. Geuzebroek, A. E. Wiskerke, M. G. Tenner, A. W. Kleyn, S. Stolte and A. Namiki, *J. Phys. Chem*, 1991, **95**, 8409.
61. M. G. Tenner, F. H. Geuzebroek, E. W. Kuipers, A. E. Wiskerke, A. W. Kleyn and S. Stolte, *Chem. Phys. Lett.*, 1990, **168**, 45.

Table of Contents

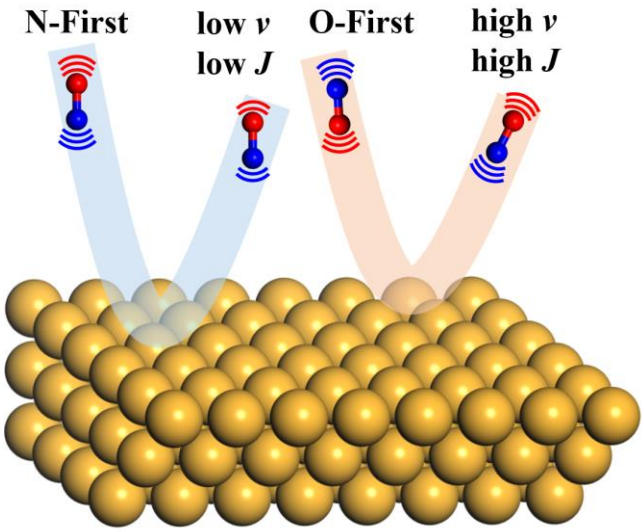

Orientation dependent energy transfer in NO(v=3) scattered from Au(111) reproduced by theory for the first time